Analysis of refraction and scattering image artefacts in x-ray analyzer-based imaging

Li-Ming Zhao(赵立明)[1], Tian-Xiang Wang(王天祥)[1], Run-Kang Ma(马润康)[1], Yao Gu(顾瑶)[1], Meng-Si Luo(罗梦丝)[1], Heng Chen(陈恒)[1], Zhi-Li Wang(王志立)[1,†], and Xin Ge(葛昕)[2]

[1] *Department of Optical Engineering, School of Physics, Hefei University of Technology, Anhui* 230009, *China*
[2] *Institute of Biomedical Engineering, Shenzhen Bay Laboratory, Shenzhen* 518067, *China*

(Received 21 January 2022; revised manuscript received 6 April 2022; accepted manuscript online 20 April 2022)

X-ray analyzer-based imaging (ABI) is a powerful phase-sensitive technique that can provide a wide dynamic range of density and extract useful physical properties of the sample. It derives contrast from x-ray absorption, refraction, and scattering properties of the investigated sample. However, x-ray ABI setups can be susceptible to external vibrations, and mechanical imprecisions of system components, e.g., the precision of motor, which are unavoidable in practical experiments. Those factors will provoke deviations of analyzer angular positions and hence errors in the acquired image data. Consequently, those errors will introduce artefacts in the retrieved refraction and scattering images. These artefacts are disadvantageous for further image interpretation and tomographic reconstruction. For this purpose, this work aims to analyze image artefacts resulting from deviations of analyzer angular positions. Analytical expressions of the refraction and scattering image artefacts are derived theoretically and validated by synchrotron radiation experiments. The results show that for the refraction image, the artefact is independent of the sample's absorption and scattering signals. By contrast, artefact of the scattering image is dependent on both the sample's refraction and scattering signals, but not on absorption signal. Furthermore, the effect of deviations of analyzer angular positions on the accuracy of the retrieved images is investigated, which can be of use for optimization of data acquisition. This work offers the possibility to develop advanced multi-contrast image retrieval algorithms that suppress artefacts in the retrieved refraction and scattering images in x-ray analyzer-based imaging.

Keywords: x-ray imaging, analyzer-based imaging, image artefacts

PACS: 87.59.–e, 42.30.Va, 87.57.N– **DOI:** 10.1088/1674-1056/ac685d

1. Introduction

X-ray phase-contrast imaging has gained popularity owing to the ability of imaging weakly absorbing objects with a high contrast at high x-ray energies. In hard x-ray regime, the sensitivity of phase-contrast imaging is expected to be at least two orders higher than that of absorption imaging for samples made of light elements.[1] During the past two decades, x-ray phase contrast imaging relies on several interference or analyzer methods to transform the phase shifts into measurable intensity modulations in the detector plane. These techniques include x-ray crystal interferometer,[2] analyzer-based imaging,[3–6] propagation-based imaging,[7] grating-based interferometric imaging[8–14] and edge-illumination imaging.[15,16] In recent years, the great potential of x-ray analyzer-based imaging has been explored, including but not limited to noninvasive soft tissue engineering,[17] functional lung imaging,[18] damage evolution,[19] detection of 3D printing technology,[20] measuring the airway size of emphysema[21] and imaging of fresh agricultural products.[22]

In x-ray analyzer-based imaging, x-ray refraction and scattering images have been demonstrated to provide complementary information to conventional attenuation-based radiography and computed tomography.[23] However, the sample's absorption, refraction, and scattering signals are measured simultaneously in the acquired radiographic images.[24] This information superposition can make the image interpretation ambiguous in practical applications. Therefore, several algorithms have been developed in order to separate the three different signals and accurately quantify them.[5,25–32] Quite recently, Gaussian generalized diffraction enhanced imaging (G^2DEI) algorithm has been presented to retrieve the absorption, refraction, and scattering properties of an object by use of only three intensity measurements.[31] Owing to the extended angular acceptance range, G^2DEI algorithm is expected to be a quantitative characterization tool with sufficient structural sensitivity on a submicron length scale.[31] Previous studies demonstrated that precise angular positioning of the analyzer crystal within sub-arcseconds was indispensable for the precise detection of phase shifts.[33] However, external vibrations of experimental environments, as well as mechanical imprecisions of system components, e.g., the precision of motor, can induce deviations of analyzer angular positions, and hence errors in the acquired raw data.

Image artefacts will deteriorate image quality, and hence hinders future practical applications of x-ray analyzer-based imaging. Therefore, it becomes quite necessary to quantify the

[†]Corresponding author. E-mail: dywangzl@hfut.edu.cn

© 2023 Chinese Physical Society and IOP Publishing Ltd

refraction and scattering image artefacts resulting from deviations of analyzer angular positions. To the best of our knowledge, this topic has not been adequately studied in previous literatures. We note that in x-ray grating interferometry, stepping errors due to external vibration, thermal drift or mechanical inaccuracies will cause obvious Moiré artefacts in the retrieved refraction and dark-field images.[34] Theoretical expressions of Moiré artefacts were derived by using a Taylor series expansion. Based on those expressions, a simple algorithm was presented for correction and removal of these artefacts.[35] Laboratory experimental results confirmed the feasibility of the algorithm.

In this work, we present analysis of image artefacts resulting from deviations of analyzer angular positions. For refraction and scattering retrieval, we consider the G^{2}DEI algorithm.[31] A Taylor series expansion is utilized to establish theoretical models to correlate deviations of analyzer angular positions with artefacts in the retrieved refraction and scattering images. Finally, theoretical models are verified by synchrotron radiation experiments and the obtained results are discussed. The results of this work can be useful for further development of advanced algorithms to suppress image artefacts, and for correct image interpretation, especially in applications of in-laboratory x-ray analyzer-based imaging instruments.[36–38]

2. Theoretical analysis of image artefacts

In the following, we will theoretically analyze the correlation between deviations of analyzer angular positions and artefacts in the refraction and scattering images retrieved by G^{2}DEI algorithm. As detailed explained by Aefelli *et al.*,[31] the G^{2}DEI algorithm can be traced back to the fact that the sample's refraction generates a shift of the center of the local rocking curve by $\Delta\theta_{\mathrm{R}}$, while Gaussian scattering with a standard deviation σ_{s}^2 increases the width of the measured local rocking curve.[25,26] The power of G^{2}DEI algorithm relies on the Gaussian approximation of the measured rocking curve (RC). Under this approximation, three intensity measurements are acquired at three well separated analyzer angular positions for multi-contrast image retrieval. When the analyzer is set to a given angular position θ_i, the intensity measured by the detector $I(\theta_i)$ can be written as follows:[29,31,39,40]

$$I(\theta_i) = I_{\mathrm{R}} \cdot \sqrt{\frac{\sigma^2}{\sigma_{\mathrm{s}}^2+\sigma^2}} \cdot \exp\left[-\frac{1}{2}\frac{(\theta_i+\Delta\theta_{\mathrm{R}})^2}{(\sigma_{\mathrm{s}}^2+\sigma^2)}\right], \tag{1}$$

where σ^2 is the standard deviation of Gaussian approximated intrinsic rocking curve. Equation (1) contains three unknown parameters, including the absorption I_{R}, the refraction $\Delta\theta_{\mathrm{R}}$, and the scattering σ_{s}^2. With three acquired intensity measurements $I(\theta_i)$ $(i=1,2,3)$, the G^{2}DEI algorithm allows quantitatively retrieval of the refraction and scattering signals on a pixel-by-pixel basis,

$$\Delta\theta_{\mathrm{R}} = \frac{\ln\left[\frac{I(\theta_3)}{I(\theta_2)}\right]\cdot(\theta_2^2-\theta_1^2) - \ln\left[\frac{I(\theta_1)}{I(\theta_2)}\right]\cdot(\theta_2^2-\theta_3^2)}{2\left\{\ln\left[\frac{I(\theta_1)}{I(\theta_2)}\right]\cdot(\theta_2-\theta_3) - \ln\left[\frac{I(\theta_3)}{I(\theta_2)}\right]\cdot(\theta_2-\theta_1)\right\}}, \tag{2}$$

$$\sigma_{\mathrm{s}}^2 = \frac{(\theta_2-\theta_1)\cdot(\theta_2-\theta_3)\cdot(\theta_1-\theta_3)}{2\left\{\ln\left[\frac{I(\theta_1)}{I(\theta_2)}\right]\cdot(\theta_2-\theta_3) - \ln\left[\frac{I(\theta_3)}{I(\theta_2)}\right]\cdot(\theta_2-\theta_1)\right\}} - \sigma^2. \tag{3}$$

For further analysis, we define $\Delta\theta_i$ $(i=1,2,3)$ as deviations of analyzer angular positions with respect to the target positions. A Taylor series expansion is used to examine the effects of deviations $\Delta\theta_i$ on retrieved refraction and scattering images. In the case of slight analyzer angular position deviations, a Taylor series expansion can be reasonably truncated after the first order. This results in the following approximation of the influence of analyzer angular position deviations $\Delta\theta_i$ on the retrieved refraction $\Delta\theta_{\mathrm{R}}$:

$$\Delta(\Delta\theta_{\mathrm{R}}) = \sum_{i=1}^{3}\frac{\partial\Delta\theta_{\mathrm{R}}}{\partial\theta_i}\cdot\Delta\theta_i, \tag{4}$$

where $\Delta(\Delta\theta_{\mathrm{R}})$ is specified as the refraction image artefact. By use of Eqs. (1) and (2), the derivative of the refraction image with respect to analyzer angular positions θ_i can be calculated as follows:

$$\frac{\partial\Delta\theta_{\mathrm{R}}}{\partial\theta_1} = \frac{(\theta_2-\theta_3)\cdot(\theta_2+\theta_3+2\Delta\theta_{\mathrm{R}})\cdot(\theta_1+\Delta\theta_{\mathrm{R}})}{(\theta_2-\theta_1)\cdot(\theta_2-\theta_3)\cdot(\theta_1-\theta_3)}, \tag{5}$$

$$\frac{\partial\Delta\theta_{\mathrm{R}}}{\partial\theta_2} = -\frac{(\theta_1-\theta_3)\cdot(\theta_3+\theta_1+2\Delta\theta_{\mathrm{R}})\cdot(\theta_2+\Delta\theta_{\mathrm{R}})}{(\theta_2-\theta_1)\cdot(\theta_2-\theta_3)\cdot(\theta_1-\theta_3)}, \tag{6}$$

$$\frac{\partial\Delta\theta_{\mathrm{R}}}{\partial\theta_3} = -\frac{(\theta_2-\theta_1)\cdot(\theta_2+\theta_1+2\Delta\theta_{\mathrm{R}})\cdot(\theta_3+\Delta\theta_{\mathrm{R}})}{(\theta_2-\theta_1)\cdot(\theta_2-\theta_3)\cdot(\theta_1-\theta_3)}. \tag{7}$$

Substituting Eqs. (5)–(7) into Eq. (4) yields the following analytical expression of the refraction image artefact:

$$\Delta(\Delta\theta_{\mathrm{R}}) = \frac{A\cdot\Delta\theta_1 + B\cdot\Delta\theta_2 + C\cdot\Delta\theta_3}{(\theta_2-\theta_1)\cdot(\theta_2-\theta_3)\cdot(\theta_1-\theta_3)} \tag{8}$$

with $A=(\theta_2-\theta_3)\cdot(\theta_2+\theta_3+2\Delta\theta_{\mathrm{R}})\cdot(\theta_1+\Delta\theta_{\mathrm{R}})$, $B=(\theta_3-\theta_1)\cdot(\theta_3+\theta_1+2\Delta\theta_{\mathrm{R}})\cdot(\theta_2+\Delta\theta_{\mathrm{R}})$ and $C=(\theta_1-\theta_2)\cdot(\theta_2+\theta_1+2\Delta\theta_{\mathrm{R}})\cdot(\theta_3+\Delta\theta_{\mathrm{R}})$.

Analogous to Eq. (4), the scattering image artefact $\Delta(\sigma_{\mathrm{s}}^2)$ induced by deviations of analyzer angular positions can be approximated by

$$\Delta(\sigma_{\mathrm{s}}^2) = \sum_{i=1}^{3}\frac{\partial\sigma_{\mathrm{s}}^2}{\partial\theta_i}\cdot\Delta\theta_i. \tag{9}$$

By using Eqs. (1) and (3), we calculate the derivative of the scattering image with respect to three analyzer angular positions as

$$\frac{\partial\sigma_{\mathrm{s}}^2}{\partial\theta_1} = \frac{2\cdot(\sigma_{\mathrm{s}}^2+\sigma^2)\cdot(\theta_2-\theta_3)\cdot(\theta_1+\Delta\theta_{\mathrm{R}})}{(\theta_2-\theta_1)\cdot(\theta_2-\theta_3)\cdot(\theta_1-\theta_3)}, \tag{10}$$

$$\frac{\partial\sigma_{\mathrm{s}}^2}{\partial\theta_2} = -\frac{2\cdot(\sigma_{\mathrm{s}}^2+\sigma^2)\cdot(\theta_1-\theta_3)\cdot(\theta_2+\Delta\theta_{\mathrm{R}})}{(\theta_2-\theta_1)\cdot(\theta_2-\theta_3)\cdot(\theta_1-\theta_3)}, \tag{11}$$

$$\frac{\partial \sigma_s^2}{\partial \theta_3} = -\frac{2\cdot\left(\sigma_s^2+\sigma^2\right)\cdot(\theta_2-\theta_1)\cdot(\theta_3+\Delta\theta_R)}{(\theta_2-\theta_1)\cdot(\theta_2-\theta_3)\cdot(\theta_1-\theta_3)}. \quad (12)$$

On substitution of Eqs. (10)–(12) into Eq. (9), we obtain the following expression of the artefact of the retrieved scattering image:

$$\Delta\left(\sigma_s^2\right) = \frac{2\cdot(D\cdot\Delta\theta_1 + E\cdot\Delta\theta_2 + F\cdot\Delta\theta_3)}{(\theta_2-\theta_1)\cdot(\theta_2-\theta_3)\cdot(\theta_1-\theta_3)} \quad (13)$$

with $D=\left(\sigma_s^2+\sigma^2\right)\cdot(\theta_2-\theta_3)\cdot(\theta_1+\Delta\theta_R)$, $E=\left(\sigma_s^2+\sigma^2\right)\cdot(\theta_3-\theta_1)\cdot(\theta_2+\Delta\theta_R)$ and $F=\left(\sigma_s^2+\sigma^2\right)\cdot(\theta_1-\theta_2)\cdot(\theta_3+\Delta\theta_R)$.

3. Experimental results

To verify the analytical results of image artefacts and visualize effects of analyzer angular position deviations on the retrieved refraction and scattering images, synchrotron radiation experiments were performed at the 4W1A beamline of Beijing Synchrotron Radiation Facility.[41] As schematically shown in Fig. 1, x-ray ABI setup utilized a first Si (111) crystal to monochromize the incident x-rays. The beam with a photon energy of 15 keV was then selected and incident on the sample. The beam exiting from the sample was analyzed by a second Si (111) crystal. Finally, the intensities were recorded by a high-resolution x-ray digital camera system FDS694 by Photonic Science Ltd., which has a small pixel size of 4.5 μm. A demineralized mouse joint was used as the sample. A total of 85 intensity measurements were acquired, with the analyzer angular position ranging from −84 μrad to 84 μrad with an increment of 2 μrad. At each analyzer angular position, a flat-field image without sample was acquired. Three intensity measurements were selected and processed by the G^{2}DEI algorithm, and the retrieved refraction and scattering images served as the ground truth, and were used as inputs for calculations of Eqs. (8) and (13), respectively.

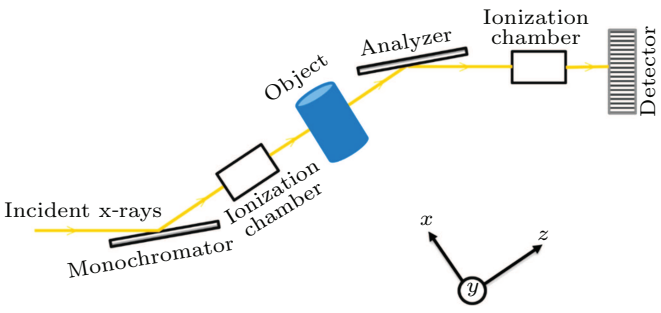


Fig. 1. Schematic diagram of x-ray ABI setup.

For the G^{2}DEI algorithm, three intensity measurements corresponding to $\theta_1=-21.3$ μrad, $\theta_2=0$ μrad and $\theta_3=23.3$ μrad were utilized for retrieval of refraction and scattering images. We assume that these three intensity measurements are acquired with analyzer angular position deviations. The values of the three analyzer angular position deviations are randomly chosen from the interval $\Delta\theta_i\in[-2,2]\times 0.1$ μrad. In the following, the superscript 'obj' is used to denote the values measured with the object in place, while the superscript 'ref' denotes the values measured as a reference without the object. The following analyzer angular position deviations are exemplarily chosen to evaluate and discuss the results of this work, including $\Delta\theta_1^{\rm obj}=0.004$ μrad, $\Delta\theta_2^{\rm obj}=0.117$ μrad and $\Delta\theta_3^{\rm obj}=0.184$ μrad for the object measurement, and $\Delta\theta_1^{\rm ref}=-0.186$ μrad, $\Delta\theta_2^{\rm ref}=0.180$ μrad and $\Delta\theta_3^{\rm ref}=0.106$ μrad for the reference measurement. However, besides these specific deviations, several other sets of analyzer angular position deviations were also used to evaluate the analytical and experimental results. And they all show equivalent results.

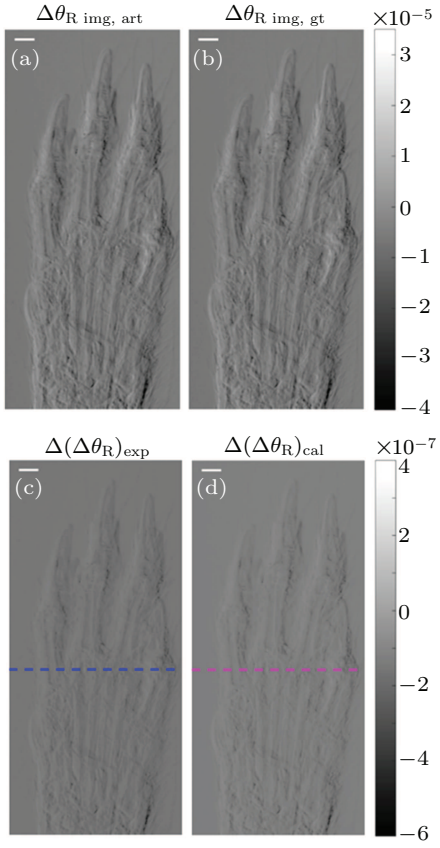


Fig. 2. (a) Experimental refraction image with artefact. (b) Experimental refraction image without artefact. (c) Experimental artefact image. (d) Calculated artefact image. Scale bar is 0.45 mm.

Defining $\theta_i+\Delta\theta_i$ $(i=1,2,3)$ as the target positions without deviations, we can retrieve the refraction image with artefacts by applying the G^{2}DEI algorithm to three measured intensities with analyzer angular position deviations. The retrieved refraction image with artefacts is shown in Fig. 2(a) (additional subscript 'img, art'). As a comparison, the corresponding refraction image without artefacts is shown Fig. 2(b) (additional subscript 'img, gt'). The pixelwise difference of Figs. 2(a) and 2(b) is calculated, and thus the artefact image resulting from analyzer angular position deviations is deduced. While Fig. 2(c) (additional subscript 'exp') shows experimen-

tal artefact image, Fig. 2(d) (additional subscript 'cal') displays the calculated artefact image by using Eq. (8) and the ground truth image. Qualitatively, the visual equivalence between Figs. 2(c) and 2(d) verifies the validity of Eq. (8) for calculating the refraction image artefact.

For a quantitative evaluation, Fig. 3 shows a line profile comparison along the line marked by the dashed line in Figs. 2(c) and 2(d). The solid blue line corresponds to the experimental result, while the magenta line corresponds to theoretically calculated result. The agreement of the two line profiles is quantitatively excellent, confirmed by that the calculated correlation coefficient has a great value of 0.9981. However, the existence of some locally minor discrepancies between experimental and calculated line profiles can be explained by the first-order truncation of the Taylor series expansion used in the derivation of Eq. (8).

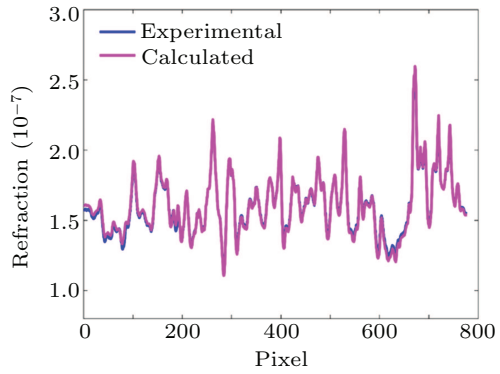


Fig. 3. Line profile comparison of refraction image artefact along the dotted line in Figs. 2(c) and 2(d).

Figure 4 shows the results of scattering images, retrieved by the G^{2}DEI algorithm using the same experimental data as Fig. 2. The scattering image with artefacts is shown in Fig. 4(a) (additional subscript 'img, art'), while the corresponding scattering image without artefacts is presented in Fig. 4(b) (additional subscript 'img, gt'), as the ground truth image for artefact image calculation. Figure 4(c) (additional subscript 'exp') displays the experimental artefact image, obtained by the difference between Figs. 4(a) and 4(b), and Fig. 4(d) (additional subscript 'cal') depicts the calculated artefact image by use of Eq. (13), Figs. 2(b) and 4(b). A qualitative comparison of Figs. 4(c) and 4(d) clearly demonstrates that theoretically calculated artefact image agrees well the experimental image.

To obtain a quantitative evaluation, Fig. 5 shows a line profile comparison of the scattering image artefacts along the dotted line in Figs. 4(c) and 4(d). Despite a few slight local deviations, the two line profiles exhibit a quantitatively good agreement, supported by a calculated correlation coefficient of 0.9862. The consistence between the two line profiles confirms the validity of theoretical models of the scattering image artefact.

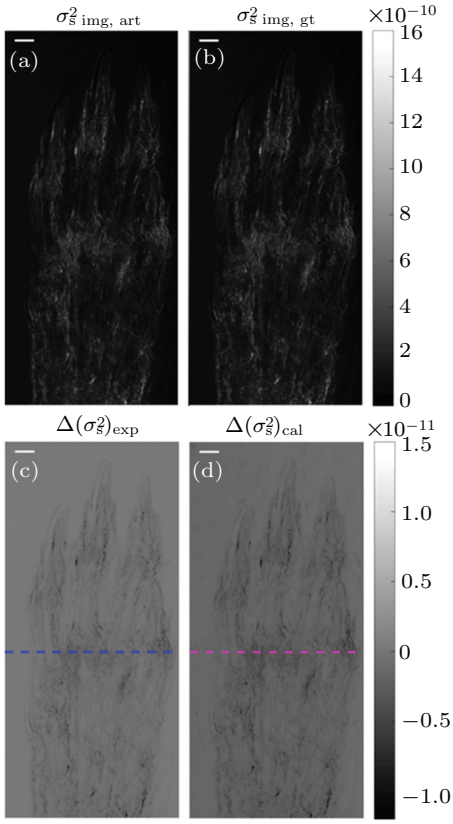


Fig. 4. (a) Experimental scattering image with artefact. (b) Experimental scattering image without artefact. (c) Experimental artefact image. (d) Calculated artefact image. Scale bar is 0.45 mm.

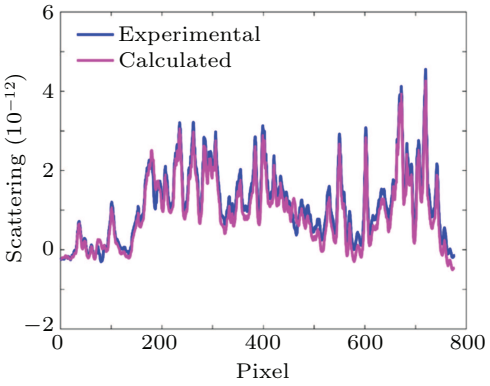


Fig. 5. Line profile comparison of scattering image artefact along the dotted line in Figs. 4(c) and 4(d).

Finally, due to stochastic nature of analyzer angular position deviations, several other sets of deviations are also investigated, and the corresponding line profile comparisons are performed. The analyzer angular position deviations used for evaluations are listed in Table 1. Note that those deviations correspond to a misalignment of less than 10% of analyzer angular intervals during intensity measurements. The calculated correlation coefficients are listed in Table 2 for refraction and scattering images, respectively.

Table 1. Several other sets of deviations in units of μrad used for evaluations.

	Deviations	1	2	3	4	5	6	7	8
Object	$\Delta\theta_1^{obj}$	–0.149	0.165	0.053	–0.006	–0.186	0.183	–0.132	0.004
	$\Delta\theta_2^{obj}$	0.126	–0.161	–0.137	0.183	0.186	0.005	–0.187	0.117
	$\Delta\theta_3^{obj}$	0.162	–0.089	0.019	–0.143	0.188	–0.043	–0.089	0.184
Reference	$\Delta\theta_1^{ref}$	0.062	–0.182	0.072	–0.025	–0.047	0.082	0.078	–0.186
	$\Delta\theta_2^{ref}$	0.140	–0.161	0.103	0.103	0.062	–0.004	0.161	0.180
	$\Delta\theta_3^{ref}$	0.174	–0.073	–0.186	0.097	–0.125	0.129	–0.143	0.106

Table 2. Calculated correlation coefficients between experimental and calculated artefacts.

	1	2	3	4	5	6	7	8
Refraction	0.9910	0.9816	0.9958	0.9886	0.9825	0.9802	0.9810	0.9981
Scattering	0.9987	0.9969	0.9839	0.9903	0.9989	0.9997	0.9818	0.9862

As summarized in Table 2, the calculated correlation coefficient has a mean value of 0.9874 with a standard deviation of 0.0071 for the refraction image artefact, and a mean value of 0.9921 with a standard deviation of 0.0074 for the scattering image artefact, respectively. Those results again confirm the good agreement between experimental results and theoretical calculations, thus validating our theoretical analysis results, i.e., Eqs. (8) and (13).

4. Discussion

Equation (8) revealed that the refraction image artefact is dependent on the three analyzer angular positions and their deviations, and also the sample's refraction. However, it is expected that the three deviations contribute differently to the magnitude of image artefact. As shown in Eq. (8), the contribution is determined by the three defined coefficients. Figure 6(a) displays the coefficients of refraction image artefact as a function of the refraction signal. For the calculations, we have used $\theta_1 = -13.6$ μrad, $\theta_2 = 1.9$ μrad and $\theta_3 = 15.5$ μrad from a recent literature.[31] These three analyzer angular positions are close to low-angle 48%, high-angle 98%, and high-angle 31%, respectively.[31] The values of the coefficients have been normalized by the term $(\theta_2-\theta_1)\cdot(\theta_2-\theta_3)\cdot(\theta_1-\theta_3)$. The results demonstrate that the magnitude of the coefficients can be comparable to that of refraction signal. Besides, the analyzer angular position deviations contribute quite differently for different features characterized by different refraction signals. And Eq. (8) can be used for predictions before experiments and experimental optimization.

Similarly, Eq. (13) showed that artefact of the scattering image is dependent on analyzer angular positions and their deviations, and both the sample's refraction and scattering, but not on absorption. However, the three angular position deviations contribute differently to the artefact magnitude. Figures 6(b) and 6(c) show the three defined coefficients as a function of refraction and scattering, respectively. The same parameters as that of Fig. 6(a) were used, and the coefficient values were also normalized. Different from Fig. 6(a), a linear behavior is observed, with a smaller value. However, noting the difference in the magnitude of refraction and scattering, the magnitude of scattering artefact can also be comparable to that of scattering signal. Moreover, the contribution of analyzer angular position deviations is quite different for different refraction and scattering. Thus, Eq. (13) provides a simple tool for error estimations and experimental optimizations.

In experimental applications, especially for laboratory x-ray analyzer-based imaging instruments, deviations of analyzer angular positions can be easily induced by vibrations and other external influences. It is difficult to increase the stability of x-ray ABI setup sufficiently in experiments. And therefore, development of enhanced retrieval algorithms becomes quite necessary, which can effectively suppress the artefacts in the retrieved refraction and scattering images. On this sense, this work provides the foundation to develop advanced multi-contrast retrieval algorithms. This will be one of our forthcoming work.

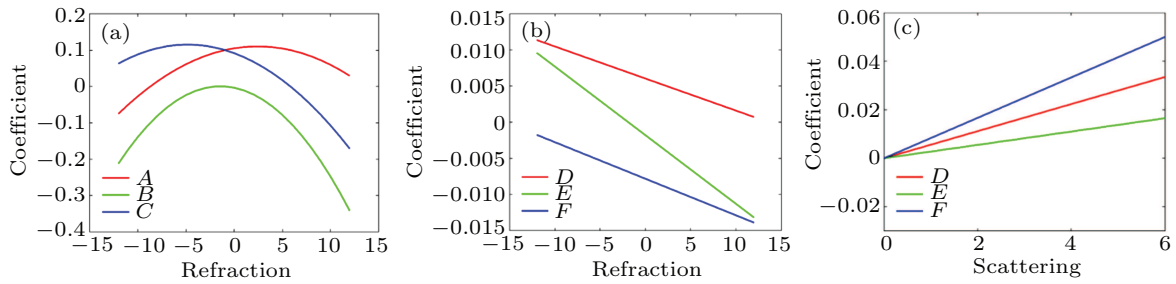


Fig. 6. (a) Coefficient of refraction image artefact as a function of refraction. (b) Coefficient of scattering image artefact as a function of refraction. (c) Coefficient of scattering image artefact as a function of scattering.

5. Conclusion

In this work, we presented analysis of refraction and scattering image artefacts resulting from analyzer angular position deviations in x-ray analyzer-based imaging. A first-order Taylor series expansion is utilized to establish theoretical models to correlate deviations of analyzer angular positions with artefacts in the retrieved refraction and scattering images. Theoretical models were validated by synchrotron radiation experiments. The results revealed that for the refraction image, the artefact was independent of the object's absorption and scattering signals. By contrast, artefacts of the scattering images were dependent on both the object's refraction and scattering signals, but not on absorption signal. The derived dependency of image artefacts on deviations of analyzer angular positions could be used to develop advanced multi-contrast image retrieval algorithms that suppress image artefacts, and for correct image interpretation especially in laboratory x-ray analyzer-based imaging instruments.

Acknowledgements

Project supported by the National Natural Science Foundation of China (Grant Nos. U1532113, 11475170, and 11905041), the Fundamental Research Funds for the Central Universities (Grant No. PA2020GDKC0024), and Anhui Provincial Natural Science Foundation, China (Grant No. 2208085MA18).

References

[1] Momose A and Fukuda J 1995 *Med. Phys.* **22** 375
[2] Momose A, Yoneyama A and Hirano K 1997 *J. Synchrotron Radiat.* **4** 311
[3] Davis T J, Gureyev T E, Stevenson A W, Wilkins S W and Gao D 1995 *Nature* **373** 595
[4] Ingal V N and Beliaevskaya E A 1995 *J. Phys. D* **28** 2314
[5] Chapman D, Thomlinson W, Johnston R E, Washburn D, Pisano E, Gmür N, Zhong Z, Menk R, Arfelli F and Sayers D 1997 *Phys. Med. Biol.* **42** 2015
[6] Chen H, Liu B, Zhao L M, Ren K and Wang Z L 2021 *Chin. Phys. B* **30** 18701
[7] Burvall A, Lundström U, Takman P, Larsson D H and Hertz H M 2011 *Opt. Express* **19** 10359
[8] Weitkamp T, Diaz A, David C, Pfeiffer F and Ziegler E 2005 *Opt. Express* **13** 6296
[9] Pfeiffer F, Weitkamp T, Bunk O and David C 2006 *Nat. Phys.* **2** 258
[10] Pfeiffer F, Bech M, Bunk O, Kraft P, Eikenberry E F, BroNnimann C, Grünzweig C and David C 2008 *Nat. Mater.* **7** 134
[11] Yashiro W, Terui Y, Kawabata K and Momose A 2010 *Opt. Express* **18** 16890
[12] Ge X, Wang Z L, Gao K, Zhang K, Hong Y L, Wang D J, Zhu Z Z, Zhu P P and Wu Z Y 2011 *Anal. Bioanal. Chem.* **401** 865
[13] Wang Z L, Gao K, Chen J, Ge X, Zhu P P, Tian Y C and Wu Z Y 2012 *Chin. Phys. B* **21** 118703
[14] Wang Z L, Gao K, Ge X, Wu Z, Chen H, Wang S H, Zhu P P, Yuan Q X, Huang W X, Zhang K and Wu Z Y 2013 *J. Phys. D* **46** 494003
[15] Olivo A, Arfelli F, Cantatore G, Longo R, Menk R H, Pani S, Prest M, Poropat P, Rigon L and Tromba G 2001 *Med. Phys.* **28** 1610
[16] Diemoz P C, Bravin A, Sztrókay-Gaul A, Ruat M, Grandl S, Mayr D, Auweter S, Mittone A, Brun E, Ponchut C, Reiser M F, Coan P and Olivo A 2016 *Phys. Med. Biol.* **61** 8750
[17] Izadifar Z, Honaramooz A, Wiebe S, Belev G, Chen X and Chapman D 2016 *Biomaterials* **82** 151
[18] Aulakh G K, Mann A, Belev G, Wiebe S, Kuebler W M, Singh B and Chapman D 2017 *Phys. Med. Biol.* **63** 015009
[19] Müeller B R, Cooper R C, Lange A, Kupsch A, Wheeler M, Hentschel M P, Staude A, Pandey A, Shyam A and Bruno G 2018 *Acta Mater.* **144** 627
[20] Laquai R, Müller B R, Kasperovich G, Haubrich J, Requena G and Bruno G 2018 *Mater. Res. Lett.* **6** 130
[21] Kitchen M J, Buckley G A, Kerr L T, Lee K L and Hooper S B 2020 *Biomed. Opt. Express* **11** 4176
[22] Takeya S, Nakano K, Thammawong M, Umeda H, Yoneyama A, Takeda T, Hyodo K and Matsuo S 2016 *Food. Chem.* **205** 122
[23] Bravin A, Coan P and Suortti P 2013 *Phys. Med. Biol.* **58** R1
[24] Diemoz P C, Coan P, Glaser C and Bravin A 2010 *Opt. Express* **18** 3494
[25] Pagot E, Cloetens P, Fiedler S, Bravin A and Thomlinson W 2003 *Appl. Phys. Lett.* **82** 3421
[26] Wernick M N, Wirjadi O, Chapman D, Zhong Z, Galatsanos N P, Yang Y, Brankov J G, Oltulu O, Anastasio M A and Muehleman C 2003 *Phys. Med. Biol.* **48** 3875
[27] Nesterets Y I, Coan P, Gureyev T E, Bravin A, Cloetens P and Wilkins S 2006 *Acta. Crys.* **A62** 296
[28] Rigon L, Arfelli F and Menk R H 2007 *Appl. Phys. Lett.* **90** 114102
[29] Majidi K, Li J, Muehleman C and Brankov J G 2014 *Phys. Med. Biol.* **59** 1877
[30] Bao Y, Wang Y, Li P Y, Wu Z, Shao Q G, Gao K, Wang Z L, Ju Z Q, Zhang K, Yuan Q X, Huang W X, Zhu P P and Wu Z Y 2015 *J. Synchrotron Radiat.* **22** 786
[31] Arfelli F, Astolfo A, Rigon L and Menk R H 2018 *Sci. Rep.* **8** 362
[32] Wang Z L, Liu D L, Zhang J, Huang W X, Yuan Q X, Gao K and Wu Z 2018 *J. Synchrotron Radiat.* **25** 1206
[33] Yoneyama A, Lwin T T and Kawamoto M 2020 *J. Synchrotron Radiat.* **27** 468
[34] Christian H, Martino L, Georg P, Marcus R, Thomas W, Thomas M, Gisela A and Ludwig R 2017 *Opt. Express* **25** 32897
[35] Fabio D M, Mathias M, Lorenz B, Peter N, Julia H and Franz P 2018 *Opt. Express* **26** 12707
[36] Chapman D, Nesch I, Hasnah M O and Morrison T I 2006 *Nucl. Instrum. Methods Phys. Res. A Accel. Spectrom. Detect. Assoc. Equip.* **562** 461
[37] Vine D J, Paganin D M, Pavlov K M, Kräußlich J, Wehrhan O, Uschmann I and Förster E 2007 *Appl. Phys. Lett.* **91** 254110
[38] Nesch I, Fogarty D P, Tzvetkov T, Reinhart B, Walus A C, Khelashvili G, Muehleman C and Chapman D 2009 *Rev. Sci. Instrum.* **80** 093702
[39] Khelashvili G, Brankov J G, Chapman D, Anastasio M A, Yang Y, Zhong Z and Wernick M N 2006 *Phys. Med. Biol.* **51** 221
[40] Yang H, Xuan R J, Hu C H and Duan J H 2014 *Chin. Phys. B* **23** 048701
[41] Yuan Q X, Zhang K, Hong Y L, Huang W X, Gao K, Wang Z L, Zhu P P, Gelb J, Tkachuk A, Hornberger B, Feser M, Yun W B and Wu Z Y 2012 *J. Synchrotron Radiat.* **19** 1021